MRI detection of single particles for cellular imaging

Erik M. Shapiro[†‡], Stanko Skrtic[†], Kathryn Sharer[†], Jonathan M. Hill[§], Cynthia E. Dunbar[§], and Alan P. Koretsky[†]

[†]Laboratory of Functional and Molecular Imaging, National Institute of Neurological Disorders and Stroke and [§]Hematology Branch, National Heart, Lung, and Blood Institute, National Institutes of Health, 9000 Rockville Pike, Bethesda, MD 20892

Communicated by Mildred Cohn, University of Pennsylvania School of Medicine, Philadelphia, PA, June 8, 2004 (received for review October 28, 2003)

There is rapid growth in the use of MRI for molecular and cellular imaging. Much of this work relies on the high relaxivity of nanometer-sized, ultrasmall dextran-coated iron oxide particles. Typically, millions of dextran-coated ultrasmall iron oxide particles must be loaded into cells for efficient detection. Here we show that single, micrometer-sized iron oxide particles (MPIOs) can be detected by MRI *in vitro* in agarose samples, in cultured cells, and in mouse embryos. Experiments studying effects of MRI resolution and particle size from 0.76 to 1.63 μm indicated that T_2^* effects can be readily detected from single MPIOs at 50-μm resolution and significant signal effects could be detected at resolutions as low as 200 μm. Cultured cells were labeled with fluorescent MPIOs such that single particles were present in individual cells. These single particles in single cells could be detected both by MRI and fluorescence microscopy. Finally, single particles injected into single-cell-stage mouse embryos could be detected at embryonic day 11.5, demonstrating that even after many cell divisions, daughter cells still carry individual particles. These results demonstrate that MRI can detect single particles and indicate that single-particle detection will be useful for cellular imaging.

Numerous recent studies (1–4) indicate that there is a wide range of applications for MRI in molecular and cellular imaging. A key requirement for these applications is the availability of high-relaxivity MRI contrast agents that have a large effect on the MRI signal. One of the agents with very high relaxivity is nanometer-sized, ultrasmall dextran-coated iron oxide particles (USPIOs). These nanometer-sized particles have a large effect on MRI signal intensities due to the fact that they are superparamagnetic and disrupt magnetic field homogeneity to an extent much larger than their size. A growing number of studies have demonstrated the usefulness of USPIOs and MRI to detect receptors (3, 5–8) and monitor cell migration (9–11). Indeed, when a cell is labeled with millions of USPIOs, single cells can be detected by MRI even though the MRI is acquired at low resolution (50–100 μm) compared with the size of the cells (5–20 μm; refs. 12–14).

A drawback of techniques that use USPIOs is that for significant signal changes, many particles need to be within an imaging voxel. Recently, we have shown that micrometer-sized iron oxide particles (MPIOs), which are commercially available, are efficiently endocytosed by a variety of cells, and these particles can be used for cellular imaging by MRI (14). Because these particles are polymer-coated and are impregnated with a fluorescent agent, it becomes possible to do both fluorescence microscopy and MRI on cells labeled with such particles. Empirical observations suggest that an iron oxide particle disrupts the magnetic field enough for MRI detectability for a distance at least 50 times its size,[¶] leading to the conclusion that cells harboring single, micrometer-sized particles should be detectable by T_2^*-weighted MRI at resolutions of $\approx$50 μm.

Here, we demonstrate that single MPIOs can be detected and used for cell labeling. Initially, we quantified image contrast as a function of particle size and various imaging parameters in phantom systems. Next, we introduced single particles into single cells and investigated the MRI effects of these particles. Finally, embryos were injected at the single-cell stage with particles and were allowed to develop to embryonic day (E)11.5. Single particles were visualized in the intact embryos with MRI and were confirmed with histological sections. The ability to detect single particles by MRI should open up new possibilities for cellular imaging.

Materials and Methods

Phantom Studies. Six samples of different iron concentrations were made for four different sizes of encapsulated superparamagnetic iron oxide particles. The concentrations were 1.0, 0.5., 0.1, 0.01, 0.001, and 0.0001 mM iron. The four samples used were Feridex, a U.S. Food and Drug Administration-approved iron oxide nanoparticle (iron core 20–30 nm), and three large iron oxide nanoparticles (0.76, 0.98, and 1.63 μm) from Bangs Laboratories (Fishers, IN). These Bangs particles are magnetite cores encapsulated with styrene/divinyl benzene with dragon green fluorescent dye (480-nm excitation, 520-nm emission) soaked in. Table 1 lists the important information regarding Feridex and the different Bangs particles. The size distribution of these particles is quite broad. For example, the largest particles (1.63 μm in diameter) have a skewed distribution, with the middle 80% of the sizes of the particles falling between 0.72 and 2.98 μm. All numbers are per the manufacturer's specifications for the specific lots delivered.

Samples were made as 4% agarose gels in sealed culture tubes. The tubes were immersed in boiling water until the agarose mixture became translucent. At this point, microtubes (4.4 mm i.d.) were inserted into the culture tubes, the culture tubes were resealed, and the tube ensemble was left to cool slowly at room temperature. Slow cooling was preferable to refrigeration because it avoided trapping air bubbles inside the sample tubes. After several hours, the culture tubes were carefully cracked and the sample-filled microtubes were pried from the agarose gel. The sample-filled microtubes were tied together with silk, were sealed, and were then immersed in agarose as a six-sample set of a single-sized particle. This procedure was performed to lessen the susceptibility artifacts at the edge of the tubes. The ensemble was refrigerator cooled to avoid remelting the samples in the microtubes.

MRI. MRI was performed on an 11.7 T horizontal bore Bruker Avance imaging system, using a 35-mm Bruker birdcage coil. Fast gradient echo, images were obtained on each set of six samples at four different resolutions (400-, 200-, and 100-μm isotropic, and 50 $\times$ 75 $\times$ 50 μm, hereafter referred to simply as 50 μm) and at two or four echo times (TEs) (5, 10, 15, and 20 ms). Other imaging parameters were: repetition time = 200 ms, one or four averages (50-μm images), and field of view = 2.56 $\times$ 1.92 $\times$ 1.28 cm. Scan times were 5 min, 20 min, 80 min, and 14.5 h for the 400-, 200-, 100- and 50-μm images, respectively. Statistical analyses (ANOVA and Student's paired *t* test) were performed in EXCEL (Microsoft) to compare the results from the different imaging experiments.

Abbreviations: USPIO, ultrasmall dextran-coated iron oxide particle; MPIO, micrometer-sized iron oxide particle; TE, echo time; E*n*, embryonic day *n*.

[‡]To whom correspondence should be addressed. E-mail: shapiroe@ninds.nih.gov.

[¶]Lauterbur, P. C., Bernardo, M. L., Jr., Mendonca Dias, M. H. & Heldman, A. W., Proceedings of the Fifth International Society for Magnetic Resonance in Medicine Meeting, Aug. 19–22, 1986, Montreal, QC, Canada, p. 229 (abstr.).

Table 1. Properties of various superparamagnetic iron oxide particles

Particle	Iron equivalent core size, μm	Picogram of iron per particle	No. of particles per gram	No. of particles for 1 nmol of iron
Feridex*	0.02–0.03	10^{-6} to 10^{-7}	NA	$\approx 10^{17}$
Bangs A	1.63	1.10	2.78×10^{11}	5.08×10^{10}
Bangs B	0.96	0.125	1.60×10^{12}	4.48×10^{11}
Bangs C	0.76	0.128	2.61×10^{12}	4.36×10^{11}

*Values are based on an estimate of thousands of iron atoms per Feridex molecule. NA, not applicable.

Hepatocyte Isolation, Culture, and Imaging. Murine hepatocytes were isolated from female C57BL/6 mice by the collagenase perfusion method, followed by repeated centrifugations according to Seglen (15). Isolated hepatocytes were suspended and cultured in DMEM/F-12 medium (GIBCO) with 5% FBS/2 mM glutamine/0.875 μM bovine insulin/100 nM dexamethasone/5 ng/ml EGF/100 units/ml penicillin/100 μg/ml streptomycin. Cells were plated at a density of 6×10^5 cells per cm^2 on plastic culture flasks (Tissue Culture, Greiner, Longwood, FL) and incubated for 10 min to 24 h with 10^2 to 10^5 0.96-μm large encapsulated superparamagnetic microspheres (Bangs Laboratories). For imaging purposes, the cells were transferred onto two-well chamber slides (Lab-Tek II, Nunc, Rochester, NY). Imaging was then performed after adhesion in an identical manner to the agarose samples except that the highest resolution image was a true 50-μm isotropic. The field of view of these samples was $2.56 \times 2.56 \times 0.64$ cm.

Fibroblast Culture and Imaging. Murine fibroblasts were purchased from American Type Culture Collection and were cultured according to the directions. Subconfluent cell cultures (75-cm^2 flasks) were labeled by an overnight incubation with 10^3 to 10^4 1.63-μm Bangs particles. Cells were then transferred onto eight-well chamber slides (Lab-Tek II, Nunc), thus achieving only a few singly labeled cells within many more unlabeled cells in each chamber. Imaging was then performed after adhesion in an identical manner to the hepatocytes, except for the following two details. Imaging was performed at 100-μm isotropic resolution and with 1 mM Magnevist (Berlex Laboratories, Wayne, NJ), a gadolinium-based contrast agent, to lower the T_1 of the bulk water to allow rapid imaging.

Embryo Injection, Growth, and Imaging. Excess female transgenic mice, bred in-house, of various ages, on a FVB or B6D2 background strain, were superovulated with 5 units of pregnant mare serum gonadotropin (Sigma), followed by 5 units of human chorionic gonadotropin (Sigma), 46–48 h later. They were placed with similar transgenic male mice for overnight mating. Single-cell embryos were collected the next morning by using standard techniques. They were placed in KSOM medium (Specialty Media, Phillipsburg, NJ), overlayed with light mineral oil, and placed in a 37°C, 5% CO_2 incubator until used.

The 1.63-μm particles, diluted in standard injection buffer (10 mM Tris·HCl/0.1 mM EDTA, pH adjusted to 7.4, filtered), were injected into the pronucleus or cytoplasm of previously collected embryos. Actual injected volumes were unknown, but swelling of the pronucleus or within cytoplasm was evidence of a successful injection. An estimation of particle number injected is 50–100 particles. Injected embryos were returned to the incubator for at least an hour before being transferred into pseudopregnant recipients. All lysed embryos were removed. Control embryos received no injection.

Oviduct transfer was performed to transfer injected embryos into pseudopregnant recipients. Postimplanted embryos were dissected at E11.5 in DMEM plus 10% FBS (BioSource International, Camarillo, CA) buffered with 25 mM Hepes (Mediatech, Herndon, VA). Upon dissection, embryos were fixed in 4% paraformaldehyde (Sigma) prepared in Ca^{2+}/Mg^{2+} free PBS (BioSource International) for 2 h.

MRI of the embryos was performed on an 7.0 T vertical bore Bruker Avance imaging system, using a 20-mm Bruker volume coil. Embryos were placed in fomblin (Ausimont, Thorofare, NJ), a perfluorinated polyether, which yields no proton signal. The 3D gradient echo images were obtained with repetition time = 30 ms, TE = 10 ms, number of averages = 30, field of view = $1.80 \times 1.80 \times 0.50$ cm, and matrix size = $512 \times 512 \times 128$. This imaging yielded a voxel resolution of $\approx$25-μm isotropic.

After imaging, the embryos were washed with saline to remove the fomblin, and were then paraffin-embedded and sliced at 20-μm thick (American HistoLabs, Gaithersburg, MD). Sections were then stained for iron (Prussian blue) with Nuclear red counterstaining (Sigma–Aldrich, St. Louis).

Fluorescent Imaging. A Zeiss LSM 410 laser-scanning confocal microscope, utilizing both fluorescence and Nomarski optics, was used to confirm the presence and number of Bangs particles in the hepatocytes. A Leica MZ FL III fluorescence stereomicroscope was used to confirm the presence and number of Bangs particles in the fibroblasts and to register the MR image to a fluorescent image. This method was also used to acquire wide-field and magnified images of the injected single-cell embryo and embryo histologic slides. To ensure that the particles in the MRI and the histology were properly registered, triangulation measurements were performed to various local anatomic landmarks in the images.

Results

Effect of MRI-Acquisition Parameters and Particle Size on Ability to Visualize Particles. The minimum MRI resolution necessary to visualize particles was investigated by acquiring MRIs at four different resolutions. Fig. 1*A* shows T_2^*-weighted MRI at two concentrations of 1.63-μm particles, 1 and 10 μM iron, and as a function of imaging resolution. These concentrations distribute the particles in $\approx$1% and 10% of the image voxels, respectively, at 50-μm resolution. These MRIs show that as the voxel size is decreased and the partial volume effects become less, single isolated dark voxels become detectable. Dark pixels using T_2^*-weighted contrast are consistent with signal loss due to magnetic field inhomogeneity induced by the MPIOs. At 400 μm, no specific spots are detectable; at 200 μm, specific dark areas can be detected, with well resolved areas apparent at 100 and 50 μm.

A quantitative analysis of the dark pixels was made. Fig. 1*B* demonstrates the size distribution and intensity changes in the image that particles at low concentration generate as a function of voxel size. At 50-μm resolution, single particles elicit an effect over 100.7 ± 5.3 μm as measured by the full width at half height, with a drop in intensity of 72.2 ± 4.3%. At 100-μm isotropic resolution, the effect is 195.7 ± 8.1 μm with an intensity drop of 49.9 ± 7.5%. At 200-μm isotropic resolution, the width at half height is 326.4 ± 37.5 μm with an intensity loss of 16.9 ± 4.0%. ANOVA of these data proved significant with $P < 0.01$ for all three data sets.

Three particle sizes were tested for their ability to produce MRI-visible artifacts. Fig. 2*A* shows MRIs of 0.76-, 0.96-, and 1.63-μm particles at 50-μm resolution and with a 10-ms TE. The concentrations are such that at this resolution, each sample has single particles in $\approx$10% of the voxels. The artifact sizes in these images scale with the size of the particles as indicated in Fig. 2*B*. Individual particles can be detected, with the greatest signal changes visible with the largest particles. The images in Fig. 2*A* were all acquired with a TE of 10 ms. Increasing the TE is expected to increase the apparent size and magnitude of the

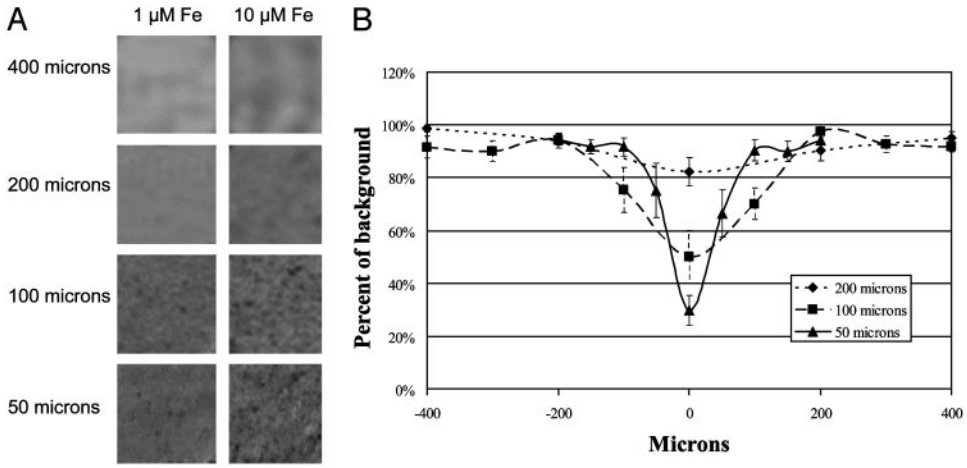

Fig. 1. Effect of image resolution on the ability to visualize individual 1.63-μm iron oxide particles. The TE was 10 ms for all experiments. (*A*) Images as the resolution is increased from 400- to 50-μm isotropic. Individual particles are resolvable at 100-μm resolution and lower. (*B*) Profile plots of seven randomly selected spots at 200-, 100-, and 50-μm resolutions, measuring the linear size of contrast regions in micrometers (*x* axis) and amount of contrast (*y* axis). Error bars are $\pm$ 1 SD. All images are 3.5- $\times$ 3.5-mm excerpts.

effects of the particles. Images acquired at twice the TE (20 ms) show that the signal intensity of the 1.63-μm particles decreased an additional 19.5%, and the width at half height of the particle increased 8.1% (data not shown).

***In Vitro* Cell Labeling and Single-Cell and Particle Detection.** To demonstrate that single MPIOs can be detected by MRI and are useful for cellular imaging, cultured cells were labeled with single particles. Fig. 3*A* shows a low-magnification view of primary hepatocytes where one can see a near confluent culture with only a fraction of the cells labeled with single, fluorescent particles. Fig. 3*B* shows a high-magnification view of a hepatocyte showing the single 0.96-μm particle that was endocytosed into this cell. Fig. 3*C* shows an MRI obtained at 50-μm resolution from a different culture labeled with single particles. Dark spots correspond to signal loss due to the presence of particles. Consistent with data presented in Fig. 1, significant loss of signal intensity occurs at distances up to 350 μm. Fig. 3*D* shows an expanded region of the image in Fig. 3*C*. Intensity decreases due to the particles are clearly detected. A single superparamagnetic particle is expected to give a characteristic shape when detected by MRI (16). The predicted barbell like shape can be seen in the images in Fig. 3*D* with decreases in signal extending further along the B_0 direction (up and down).

Fig. 4 shows a comparison between an MRI-detected region of a culture dish of a different cell type, mouse embryonic fibroblasts, labeled with single particles and a corresponding fluorescence image of the same region. MRI was acquired at 100-μm resolution in this case. Due to this lower resolution, partial voluming reduces the barbell-shaped contrast observed at high resolution to a more uniformly circular area. Circles corresponding to significant decreases in MRI signal intensity are registered to fluorescence spots of the correct size and intensity to arise from the MPIOs. It is difficult to make a rigorous comparison of these particles detected by both MRI and fluorescence stereomicroscopy. Arrows indicate potential sources of artifacts in both the MRI and the fluorescence image. Small, less-intense dark spots are due to unlabeled cells that can be detected due to the gadolinium-based contrast agent added to the medium, which causes a small susceptibility difference.

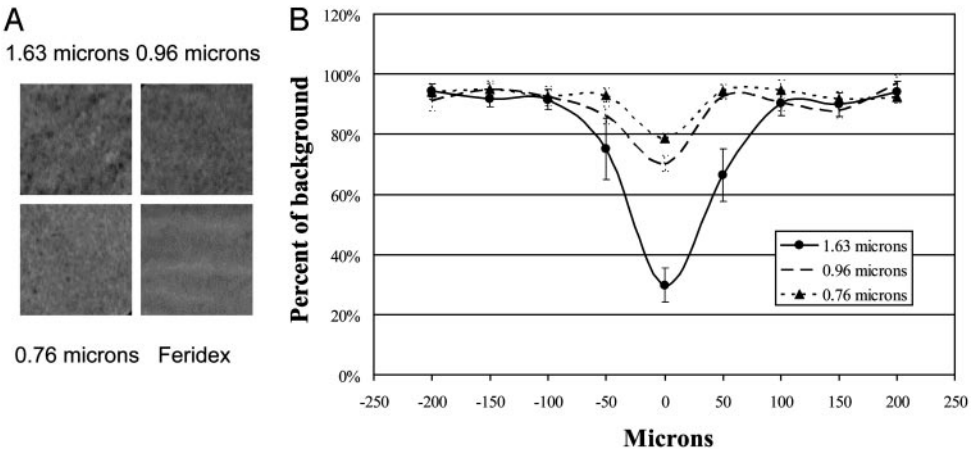

Fig. 2. Effect of particle size on the ability to visualize individual iron oxide particles. The concentration of particles was set so that in each sample $\approx$10% of the voxels contained a single particle. The TE was 10 ms and the image resolution was 50 μm for all experiments. (*A*) Images as the particle size is increased from 0.76 to 1.63 μm. Individual particles are robustly resolvable for the three sizes of particles. (*B*) Profile plots of seven random averaged contrast regions for the three sizes of particles, measuring the linear size of contrast regions in micrometers (*x* axis) and amount of contrast (*y* axis). Error bars are $\pm$ 1 SD. All images are 3.5- $\times$ 3.5-mm excerpts.

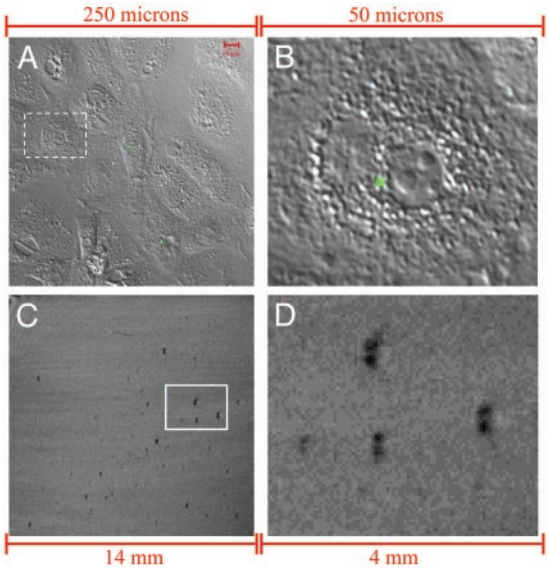

Fig. 3. Optical and magnetic resonance images of single particles in single live mouse hepatocytes. (*A*) A wide-field confocal fluorescence image superimposed on a Nomarski optics image of a nearly confluent dish of live hepatocytes, showing few single-labeled cells. (*B*) An expansion of one of the singly labeled cells (dashed box in *A*). Note the single green fluorescent spot in the cytoplasm. (*C*) An MRI of the entire culture dish with singly labeled hepatocytes. (*D*) An expansion of the boxed region in *C*. Note the characteristic barbell-shaped contrast caused by the single particle.

The large fluorescent spot in the fluorescence image is likely a piece of dust. It may also be that some iron oxide particles do not have sufficient fluorescence for detection, and some fluorescent particles contain no iron oxide.

Imaging Particles in Intact E11.5 Rat Embryos. A major advantage of being able to detect single particles for cell labeling is that when cell division dilutes particles to either one particle or no particles, the cells that harbor only single particles can still be detected. To demonstrate this hypothesis and also show that these particles might be useful for tracking developmental changes, we injected single-cell embryos with many particles. Fig. 5*A* shows a fluorescence image of a single-cell embryo after having had 1.63-μm particles injected into it. These embryos were reimplanted and developed until E11.5, where they were then removed and fixed.

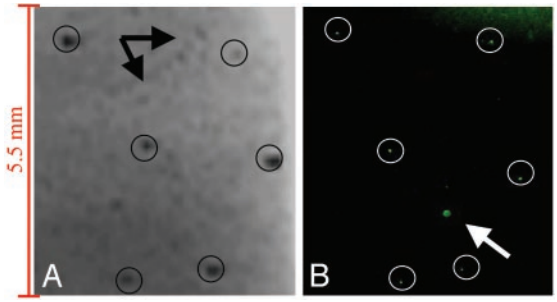

Fig. 4. Magnetic resonance and optical images of single particles in single live mouse fibroblasts. (*A*) MRI of a culture slide with few singly labeled fibroblasts. (*B*) The corresponding fluorescent stereomicroscope image of the same slide as in *A*. Circles show the correspondence of MRI and fluorescently detected MPIOs. Arrows indicate sources of artifacts, which include slight darkening in the MRI of unlabeled cells that exclude the gadolinium contrast agent (black arrows in *A*), and a large fluorescent contaminant in *B* (white arrow) most likely due to dust.

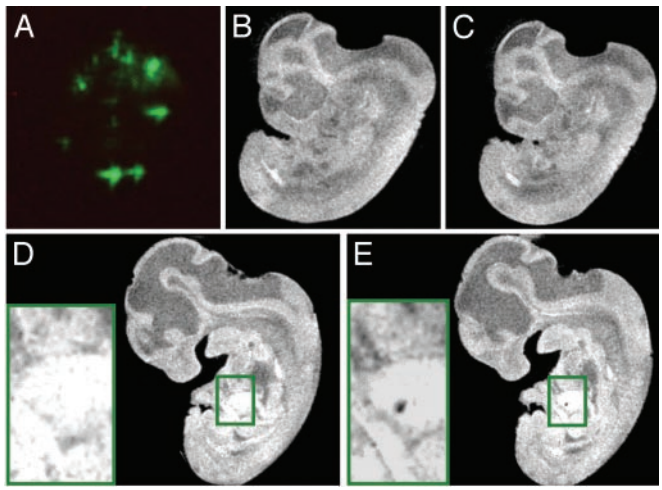

Fig. 5. Development of mouse embryos injected with MPIOs. (*A*) A fluorescent stereomicroscope image of a single-cell embryo after injection with 1.63-μm MPIOs. (*B* and *C*) Two slices from a 3D MRI data set of a control E11.5 embryo, separated by 100 μm. (*D* and *E*) Paired MRI slices of an embryo, separated by 100 μm, previously injected at the single-cell stage with 1.63-μm MPIOs. (*Insets*) Boxed areas are magnified to show signal intensity loss due to an MPIO, which is only present in *E*. Signal loss is not present in *D*. Each embryo image is ≈2 mm from head to tail. Criteria for deciding whether a dark spot is due to a particle or to background contrast include analyzing adjacent slices to ensure the contrast is punctuated.

Fig. 5 *B* and *C* are slices from a 3D MRI data set of a control E11.5 embryo, showing no punctuated dark areas. Fig. 5*E* is a slice from a 3D MRI data set of an embryo, previously injected with MPIOs, showing a punctuated, dark, susceptibility-induced contrast region in the developing gut. Fig. 5*D* shows a slice from the same data set, separated from Fig. 5*E* by 100 μm. The dark spot detected in Fig. 5*E* is absent in the slice 100 μm away (Fig. 5*D*), as well as the slice 100 μm away in the other direction (data not shown), indicating the focal nature of these hypointense signals. This evaluation is critical in deciding whether dark contrast is the result of an MPIO or due to background contrast.

To confirm that the signal loss was due to single MPIOs, embryos were sectioned for histology after MRI. Sections were stained with Prussian blue and Nuclear red counterstaining. Fig. 6 shows three MRI slices from embryos with matching histological sections. Fig. 6*A* shows a single Bangs particle in the wall of the developing intestine. Fig. 6*B* shows a single Bangs particle in the developing midsection. Fig. 6*C* displays a single Bangs particle in the lower back. In each case, there is a clear loss in MRI signal intensity that corresponds with a blue spot in the histology, indicating that the loss of signal in the MRI is due to the presence of an MPIO. Triangulation of the particles to the same discernable landmarks in the MRI and histology revealed that measured distances to the same landmark were always within 5% between the two modalities. In fact, for the three slices shown, the average measurement difference between the two modalities, for nine total measurements, was ≈1%, with the difference in the SD at ≈2%.

Discussion

MRI is generally considered an insensitive spectroscopic and imaging technique. However, increases in magnetic field strength and optimization of detector sensitivity are pushing MRI spectroscopic analysis of analytical samples down to nanomolar concentrations. Furthermore, MRI is beginning to routinely generate images at resolution of 100 μm or better in small live animals (17, 18), and a few hundred micrometers in humans (19). MRI contrast in soft tissue is excellent due to the different

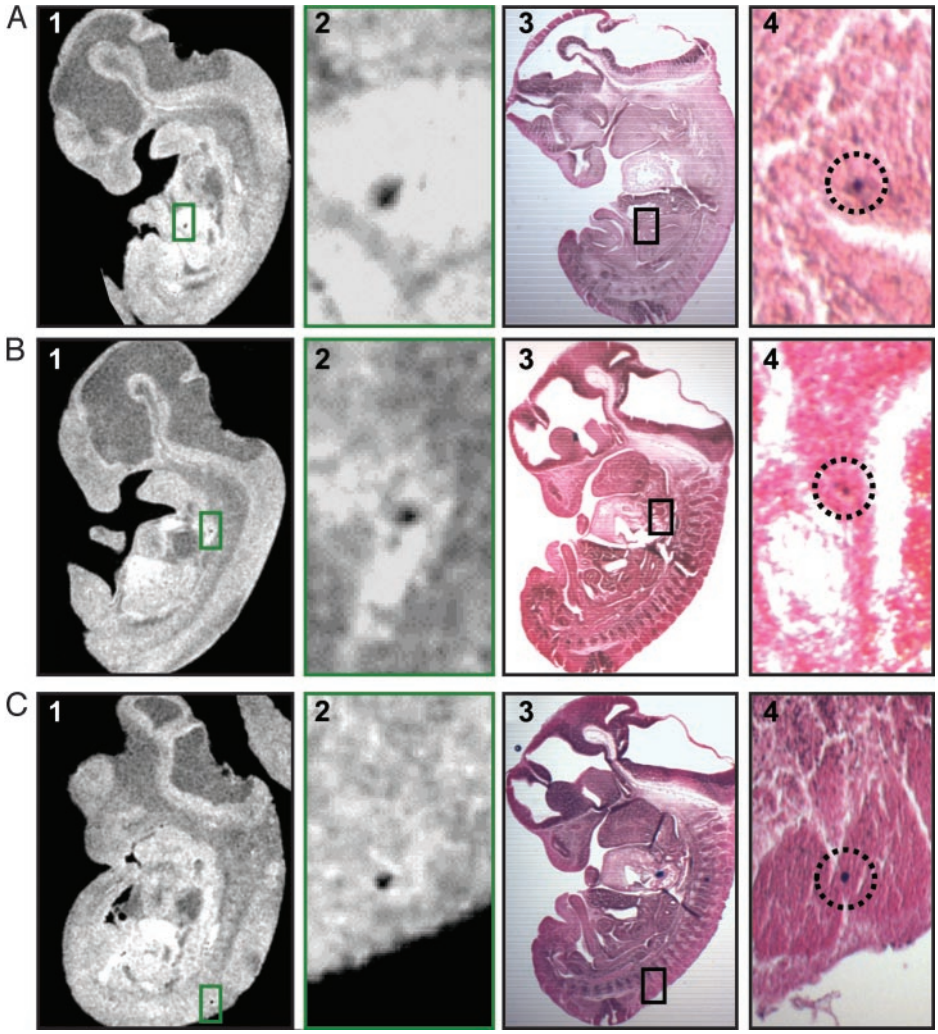

Fig. 6. MRI and histology of Bangs particles in E11.5 embryos. (*A–C*) (*A1–C1*) Slices from 3D MRI data sets. (*A2–C2*) Expansions of the boxed regions in *A1–C1*, showing susceptibility-induced contrast regions in each image. (*A3–C3*) Matching histological sections that correspond to the same plane as the accompanying MRIs. (*A4–C4*) A second set of images of the sections in *A3–C3*, acquired with a higher magnification, approximately representing the boxed regions. The stains from the individual particles are circled to assist visualization in the histology. Shown are single 1.63-μm particles registered to the areas of dark contrast in the MRIs. Each embryo image is ≈6.75 mm from head to tail, both in the MRI and in the histology. All *Insets* are ×10 magnifications.

properties of water in different tissues. Despite this imaging ability, the application of contrast agents is still important for increasing the sensitivity and specificity of MRI.

Nanometer-sized USPIOs are having an impact in molecular and cellular imaging due to their ability to alter MRI signal intensities. Major applications include targeting specific receptors and after cell migration. Typically, cells are isolated and labeled with iron oxide particles and are then reintroduced in the animal. Over the past few years, a variety of cell-labeling strategies have been developed that rely on endocytosis or strategies to enhance endocytosis (20–22). These techniques now enable a large variety of cells to be labeled effectively to detect distributions of cells by MRI. Indeed, the large effects of USPIOs allow single cells to be imaged *in vitro* (12–14), and as few as three to 50 cells have been detected *in vivo* (11, 23). However, due to the need to get millions of USPIOs into cells to get effective labeling, there are fewer successful strategies to load cells *in vivo*. One successful technique makes use of the fact that USPIOs can be efficiently endocytosed to monitor macrophage accumulation in animal models (24, 25), and potentially in humans (26). The two major drawbacks of using USPIOs are that detection requires millions of particles to concentrate in a specific voxel, and cell divisions can dilute the label below detectability. Published data (27, 28) indicate that cell labeling by using small iron oxide particles or magnetodendrimers can achieve cellular iron concentrations of 10–30 pg, which places the detectability level at 7–10 cell divisions. This finding is based on the fact that a single 0.96-μm particle has ≈0.1 pg of iron and detectability below that level begins to get challenging.

A strategy to overcome these problems as well as extend present MRI techniques would be to image single particles. In this way, only one particle would have to be delivered to a cell (or receptor) and cell divisions cannot dilute the label. Previous work (14) showed that MPIOs are effectively endocytosed by a variety of cells, and once labeled, these cells could be detected by MRI. Theory predicts that the larger the iron oxide particle, the larger the effects on T_2^*-weighted MRI (29) and that as the particle reaches micrometer size, individual particles should be detectable at ≈50-μm resolution[¶]. The results presented here clearly demonstrate that readily detectable signal effects occur from micrometer-sized particles in agarose phantoms, and from single particles in cultured cells and in intact embryos. The results from the cultured cells and the embryo injections show the potential for single particle MRI to solve the problems of needing large numbers of particles for efficient labeling

of cells and demonstrate that particles can be inherited for many cell divisions. The fact that the embryos developed normally after many particles were injected into single-cell embryos indicates that the specific MPIOs used are not toxic, which is consistent with previous work looking at viability of labeled cultured cells (14).

A major drawback of using iron-oxide-based MRI contrast agents is that the largest effect is on T_2^*, leading to signal loss. There are other causes for signal loss leading to potential artifacts. The majority of current work has focused on increasing the number of particles to increase the T_2^* effect. Another way to increase this effect is to increase the size of the particles and this forms the basis of using MPIOs. The size of the effect on MRI should grow as the radius of particle to the third power and thus any increase in particle size increases its MRI detectability. This effect was illustrated over the range of sizes from 0.76 to 1.63 μm. It will be interesting to see whether even larger particles can be effectively endocytosed by cells. Another feature of using single particles for cellular MRI is that the images at high resolution define a complex pattern of signal loss and signal increases, giving rise to a characteristic barbell shape. Evidence for this conclusion can be seen in Fig. 3. The details of the signal intensities have been theoretically derived for a single dipole in a homogeneous magnetic field (16). The signal changes detected qualitatively agree with these predictions. Indeed, in the slices above the particle, an even more complex signal pattern is observed, with the slice two above the particle (100 μm above) appearing as four bright spots surrounding the particle (data not shown). Due to the fact that a single particle is imaged, the predicted barbell distribution should be detectable, and could be used to separate signal changes due to particles from other sources of signal loss.

There are at least two major applications that can be foreseen for using MPIOs for single-particle detection by MRI. The first application is tracking cell migration and cell division, for example, by using stem cells. It is possible to label stem cells with iron oxide particles and inject them into an area of interest and follow their migration (9, 11, 30). Stem cells are highly proliferative, and cell division can dilute the label within only a few cell divisions. It has recently been shown that in dividing bone-marrow-derived stem cells heavily labeled with MPIOs, the label distributes evenly between daughter cells (14). As single particles can be visualized, it may be that more divisions can be followed. Even after MPIOs are diluted to a single particle per cell, the fate of the daughter cell that still retain the particle can be followed as demonstrated in the results from the embryos.

The second potential application of visualizing single particles in single cells is the possibility of labeling cells *in vivo*. The only cells that have been labeled with USPIOs in an intact animal are macrophages (31–35). *In vivo* targeting of USPIOs to cells is hampered by the need to effectively deliver millions of particles. With MPIOs, only a single particle should be necessary for detection by MRI, thus it should be possible to target MPIOs to a variety of cells *in vivo*.

In conclusion, single MPIOs can be detected by MRI using imaging conditions well suited to studying live animals. The specific MPIOs used here can be used to label a variety of mammalian cells, and single cells that have been labeled with single particles can be detected with MRI. The large size of the MRI signal changes induced by these particles suggest that once labeled, a daughter cell will always carry the label, and the need to have only a single particle delivered to a cell should open numerous future possibilities for cellular imaging by MRI.

We thank Dr. H. Douglas Morris (National Institutes of Health Magnetic Resonance Facility) for assistance with acquiring the MRIs of the mouse embryos and Dr. Christian A. Combs (National Heart, Lung, and Blood Institute Light Microscopy Core Facility) for assistance with acquiring the fluorescence images.

1. Massoud, T. F. & Gambhir, S. S. (2003) *Genes Dev.* **17,** 545–580.
2. Weissleder, R. (2002) *Nat. Rev. Cancer* **2,** 11–18.
3. Lanza, G. M., Abendschein, D. R., Yu, X., Winter, P. M., Karukstis, K. K., Scott, M. J., Fuhrhop, R. W., Scherrer, D. E. & Wickline, S. A. (2002) *Acad. Radiol.* **9,** Suppl. 2, S330–S331.
4. Bulte, J. W., Duncan, I. D. & Frank, J. A. (2002) *J. Cereb. Blood Flow Metab.* **22,** 899–907.
5. Renshaw, P. F., Owen, C. S., Evans, A. E. & Leigh, J. S., Jr. (1986) *Magn. Reson. Imaging* **4,** 351–357.
6. Anderson, S. A., Rader, R. K., Westlin, W. F., Null, C., Jackson, D., Lanza, G. M., Wickline, S. A. & Kotyk, J. J. (2000) *Magn. Reson. Med.* **44,** 433–439.
7. Gupta, H. & Weissleder, R. (1996) *Magn. Reson. Imaging Clin. N. Am.* **4,** 171–184.
8. Li, K. C. & Bednarski, M. D. (2002) *J. Magn. Reson. Imaging* **16,** 388–393.
9. Bulte, J. W., Zhang, S., van Gelderen, P., Herynek, V., Jordan, E. K., Duncan, I. D. & Frank, J. A. (1999) *Proc. Natl. Acad. Sci. USA* **96,** 15256–15261.
10. Modo, M., Cash, D., Mellodew, K., Williams, S. C., Fraser, S. E., Meade, T. J., Price, J. & Hodges, H. (2002) *NeuroImage* **17,** 803–811.
11. Hoehn, M., Kustermann, E., Blunk, J., Wiedermann, D., Trapp, T., Wecker, S., Focking, M., Arnold, H., Hescheler, J., Fleischmann, B. K., *et al.* (2002) *Proc. Natl. Acad. Sci. USA* **99,** 16267–16272.
12. Dodd, S. J., Williams, M., Suhan, J. P., Williams, D. S., Koretsky, A. P. & Ho, C. (1999) *Biophys. J.* **76,** 103–109.
13. Foster-Gareau, P., Heyn, C., Alejski, A. & Rutt, B. K. (2003) *Magn. Reson. Med.* **49,** 968–971.
14. Hinds, K. A., Hill, J. M., Shapiro, E. M., Laukkanen, M. O., Silva, A. C., Combs, C. A., Varney, T. R., Balaban, R. S., Koretsky, A. P. & Dunbar, C. E. (2003) *Blood* **102,** 867–872.
15. Seglen, P. O. (1979) *J. Toxicol. Environ. Health* **5,** 551–560.
16. Kim, J. K., Kucharczyk, W. & Henkelman, R. M. (1993) *Radiology* **187,** 735–741.
17. Louie, A. Y., Huber, M. M., Ahrens, E. T., Rothbacher, U., Moats, R., Jacobs, R. E., Fraser, S. E. & Meade, T. J. (2000) *Nat. Biotechnol.* **18,** 321–325.
18. Budinger, T. F., Benaron, D. A. & Koretsky, A. P. (1999) *Annu. Rev. Biomed. Eng.* **1,** 611–648.
19. Barbier, E. L., Marrett, S., Danek, A., Vortmeyer, A., van Gelderen, P., Duyn, J., Bandettini, P., Grafman, J. & Koretsky, A. P. (2002) *Magn. Reson. Med.* **48,** 735–738.
20. Yeh, T. C., Zhang, W., Ildstad, S. T. & Ho, C. (1993) *Magn. Reson. Med.* **30,** 617–625.
21. Josephson, L., Tung, C. H., Moore, A. & Weissleder, R. (1999) *Bioconjugate Chem.* **10,** 186–191.
22. Frank, J. A., Zywicke, H., Jordan, E. K., Mitchell, J., Lewis, B. K., Miller, B., Bryant, L. H., Jr., & Bulte, J. W. (2002) *Acad. Radiol.* **9,** Suppl. 2, S484–S487.
23. Kircher, M. F., Allport, J. R., Graves, E. E., Love, V., Josephson, L., Lichtman, A. H. & Weissleder, R. (2003) *Cancer Res.* **63,** 6838–6846.
24. Dardzinski, B. J., Schmithorst, V. J., Holland, S. K., Boivin, G. P., Imagawa, T., Watanabe, S., Lewis, J. M. & Hirsch, R. (2001) *Magn. Reson. Imaging* **19,** 1209–1216.
25. Ye, Q., Yang, D., Williams, M., Williams, D. S., Pluempitiwiriyawej, C., Moura, J. M. & Ho, C. (2002) *Kidney Int.* **61,** 1124–1135.
26. Kooi, M. E., Cappendijk, V. C., Cleutjens, K. B., Kessels, A. G., Kitslaar, P. J., Borgers, M., Frederik, P. M., Daemen, M. J. & van Engelshoven, J. M. (2003) *Circulation* **107,** 2453–2458.
27. Bulte, J. W., Douglas, T., Witwer, B., Zhang, S. C., Strable, E., Lewis, B. K., Zywicke, H., Miller, B., van Gelderen, P., Moskowitz, B. M., *et al.* (2001) *Nat. Biotechnol.* **19,** 1141–1147.
28. Lewin, M., Carlesso, N., Tung, C. H., Tang, X. W., Cory, D., Scadden, D. T. & Weissleder, R. (2000) *Nat. Biotechnol.* **18,** 410–414.
29. Weisskoff, R. M., Zuo, C. S., Boxerman, J. L. & Rosen, B. R. (1994) *Magn. Reson. Med.* **31,** 601–610.
30. Hill, J. M., Dick, A. J., Raman, V. K., Thompson, R. B., Yu, Z. X., Hinds, K. A., Pessanha, B. S., Guttman, M. A., Varney, T. R., Martin, B. J., *et al.* (2003) *Circulation* **108,** 1009–1014.
31. Beckmann, N., Falk, R., Zurbrugg, S., Dawson, J. & Engelhardt, P. (2003) *Magn. Reson. Med.* **49,** 1047–1055.
32. Kanno, S., Wu, Y. J., Lee, P. C., Dodd, S. J., Williams, M., Griffith, B. P. & Ho, C. (2001) *Circulation* **104,** 934–938.
33. Bulte, J. W. & Frank, J. A. (2000) *AJNR Am. J. Neuroradiol.* **21,** 1767–1768.
34. Zhang, Y., Dodd, S. J., Hendrich, K. S., Williams, M. & Ho, C. (2000) *Kidney Int.* **58,** 1300–1310.
35. Dousset, V., Delalande, C., Ballarino, L., Quesson, B., Seilhan, D., Coussemacq, M., Thiaudiere, E., Brochet, B., Canioni, P. & Caille, J. M. (1999) *Magn. Reson. Med.* **41,** 329–333.